








Detection of rubidium and samarium in the atmosphere of the ultra-hot Jupiter MASCARA-4b

ZEWEN JIANG ^{1,2} WEI WANG ¹ GANG ZHAO ^{1,2} MENG ZHAI ³ YAQING SHI ^{1,2} YUJUAN LIU,¹
JINGKUN ZHAO ¹ AND YUQIN CHEN ¹

¹CAS Key Laboratory of Optical Astronomy, National Astronomical Observatories, Chinese Academy of Sciences, Datun Road A20, Beijing 100101, China

²School of Astronomy and Space Science, University of Chinese Academy of Sciences, Beijing 100049, China

³CAS South America Center for Astronomy, National Astronomical Observatories, Chinese Academy of Sciences, Datun Road A20, Beijing 100101, China

ABSTRACT

Ultra-hot Jupiters (UHJs) possess the most extreme environments among various types of exoplanets, making them ideal laboratories to study the chemical composition and kinetics properties of exoplanet atmosphere with high-resolution spectroscopy (HRS). It has the advantage of resolving the tiny Doppler shift and weak signal from exoplanet atmosphere and has helped to detect dozens of heavy elements in UHJs including KELT-9b, WASP-76b, WASP-121b. MASCARA-4b is a 2.8-day UHJ with an equilibrium temperature of ~ 2250 K, which is expected to contain heavy elements detectable with VLT. In this letter, we present a survey of atoms/ions in the atmosphere of the MASCARA-4b, using the two VLT/ESPRESSO transits data. Cross-correlation analyses are performed on the obtained transmission spectra at each exposure with the template spectra generated by `petitRADTRANS` for atoms/ions from element Li to U. We confirm the previous detection of Mg, Ca, Cr and Fe and report the detection of Rb, Sm, Ti+ and Ba+ with peak signal-to-noise ratios (SNRs) > 5 . We report a tentative detection of Sc+, with peak SNRs ~ 6 but deviating from the estimated position. The most interesting discovery is the first-time detection of elements Rb and Sm in an exoplanet. Rb is an alkaline element like Na and K, while Sm is the first lanthanide series element and is by far the heaviest one detected in exoplanets. Detailed modeling and acquiring more data are required to yield abundance ratios of the heavy elements and to understand better the common presence of them in UHJ's atmospheres.

Keywords: Planets and satellites: atmospheres — Planets and satellites: individual (MASCARA-4b)
— Methods: data analysis – Techniques: spectroscopic

1. INTRODUCTION

Exoplanet science has achieved great progress in characterizing the atmospheres of exoplanets, and it becomes one of the most rapidly growing fields in astronomy. Ultra-hot Jupiters (UHJs) are a special population of Jupiter-like planets with dayside temperatures higher than 2200 K. In such conditions, most molecules are dissociated into their constituent atoms. The large atmospheric scale heights of UHJs make them ideal laboratories for the study of the physical and chemical properties of exoplanet atmospheres. Among all the powerful

tools for the atmospheric characterization of exoplanets, high-resolution spectroscopy (HRS) becomes a wide-employed and efficient one, that can utilize either several strong individual lines or a few dense forests of spectral lines to search for atoms and molecules and estimate their relative abundances in the atmospheres (Snellen et al. 2010; Brogi & Line 2019). Due to much larger motion of the planets as compared to their host stars, the planetary spectra move in wavelength (or velocity) space obviously, while those from star and telluric absorption are essentially stationary, so that the atmospheric signals of an exoplanet are usually well separated from the stellar and telluric signals at high spectral resolution (Wytttenbach et al. 2015). For the same reason, HRS can provide information on the relative motions of

different species, and thus can be used to study the dynamics of planet atmospheres, which can not be realized with low-resolution spectroscopy in principal.

Dozens of atoms have been detected so far using HRS in UHJs including Na, K, Ca, Mg, Ti, Fe, Co, Ca+, Fe+, Ti+, V+, Sc+, Sr+, Ni+ and Ba+. [Hoeijmakers et al. \(2019\)](#) detected neutral atoms Fe, Mg, and Na, as well as ionized Sc+, Cr+, Y+, Fe+, and Ti+ in KELT-9 b, the hottest exoplanet discovered up to today; [Ehrenreich et al. \(2020\)](#) uncovered the asymmetric absorption of Fe signal in the terminators of WASP-76b; [Azevedo Silva et al. \(2022\)](#) reported a novel detection of Ba+ in the atmospheres of WASP-121 b and WASP-76 b. Ba+ is by far the heaviest element found in the exoplanet atmospheres.

MASCARA-4 b was identified by Multi-site All-Sky CAmeRA (MASCARA) ([Talens et al. 2017](#)) and further confirmed by photometric observations which were taken with the Chilean–Hungarian Automated Telescope(CHAT) and radial velocity measurements which were taken with FIDEOS on the ESO 1-m telescope. In addition, follow up high-resolution spectra were taken during transit with the CTIO high-resolution spectrometer (CHIRON) instrument on the Small and Moderate Aperture Research Telescope System (SMARTS) telescope to detect the Doppler shadow of the transiting object, which further confirmed that the small object was indeed transiting the bright star.

MASCARA-4 b is an UHJ with a mass of $1.675 \pm 0.241 M_{\text{Jup}}$, a radius of $1.515 \pm 0.044 R_{\text{Jup}}$ and an equilibrium temperature T_{eq} of 2250 ± 62 K with an orbital period of ~ 2.82406 d ([Dorval et al. 2020](#); [Zhang et al. 2022](#)). Thus, it is an ideal target for atmospheric characterisation given its large atmospheric scale heights and TSM ([Kempton et al. 2018](#)). Recently, [Zhang et al. \(2022\)](#) explored the chemical species in the atmosphere of this planet using the Echelle Spectrograph for Rocky Exoplanets and Stable Spectroscopic Observations (ESPRESSO [Pepe et al. 2021](#)) mounted on the Very Large Telescope (VLT), and they resolved excess absorption about $H\alpha$, $H\beta$, NaI D1&D2, CaII H&K and detected Mg, Ca, Cr, Fe, and Fe+ by the cross-correlation analysis.

Considering that quite a number of heavier elements were detected very recently in the other two UHJs WASP-76 b and WASP-121 b ([Azevedo Silva et al. 2022](#)) by re-analyzing the archive ESPRESSO data, it is worthy to perform a quick survey of atoms and ions in the atmosphere of MASCARA-4 b using the HRS technique. This letter is organized as follows. We present the details of two ESPRESSO transit observations of MASCARA-4 b and data reduction in Section 2. The data analysis

including transmission spectrum construction and atmospheric cross-correlation analysis are given in section 3. The final results and some discussions are presented in section 4.

2. OBSERVATIONS AND DATA REDUCTION

Two transits of MASCARA-4 b were observed in 2020 February 13 and 2020 March 1 with ESPRESSO under the ESO programs 0104.C-0605 (PI:WYTTENBACH). ESPRESSO is a fibre-fed ultra-stable échelle high-resolution spectrograph, mounted at the 8.2m Very Large Telescope at European Southern Observatory in Cerro Paranal, Chile ([Pepe et al. 2021](#)). This observation was carried out using the single-UT HR21 mode with a spectral resolving power $R \sim 140000$ and wavelength coverage of 380 – 788 nm. For the transit in 2020 Feb 13 (hereafter T1), a total of 96 spectra were obtained with 39 taken in transit and 57 out of transit with orbital phase Φ from -0.053 to 0.087. For the transit in 2020 Mar 1 (hereafter T2), a total of 85 spectra were achieved with 25 taken in transit and 60 out of transit, covering Φ from -0.07 to 0.066. Details of the two transits are summarized in Table 1. We used the 1D spectra from the ESO data archive, which were processed by the ESPRESSO reduction pipeline, version 2.2.1. Bias, dark, flat and bad pixels were taken into account when processing the 2D images, from which 1D spectra can be sky-subtracted and extracted. Then all the échelle orders were wavelength calibrated and stitched into a combined 1D spectra.

We corrected the telluric absorption hidden in the spectra using the ESO software `Molecfit` version 1.5.7 ([Smette et al. 2015](#); [Kausch et al. 2015](#)). `Molecfit` is a tool for modelling telluric lines using the state-of-the-art radiative transfer modelling of the Earth’s atmosphere, together with a comprehensive database of molecular parameters ([Smette et al. 2015](#)). It has been widely used recently in the HRS studies of exoplanet atmosphere(e.g., [Allart et al. 2017](#); [Seidel et al. 2020](#); [Kirk et al. 2020](#)) to best remove telluric contamination.

We adopted the input parameters for `Molecfit` as described in [Allart et al. \(2017\)](#). To achieve a good estimate and removal of telluric contamination, the fitting regions were manually chosen by visual inspection and comparisons of the observed spectra and the model telluric atmospheric transmission spectra. Note that the obtained ESPRESSO spectra are given in the solar system barycentric rest frame, which were shifted to terrestrial rest frame to fulfill the `Molecfit` requirement. As an example, we show in Fig. 1 comparisons of the observed spectrum taken on T1 and its corresponding contamination-corrected spectrum around the

Table 1. Summary of the MASCARA-4b transit observations.

	Date (UT)	Number of spectra			Exp. time (s)	Airmass range (start– T_c –end)	Mean S/N (@580 nm)	Program ID
		Total	In-transit	Out-of-transit				
T1	2020-02-13	96	39	57	360	1.99 – 1.33 – 1.91	~211	0104.C-0605
T2	2020-03-01	85	25	60	300	1.72 – 1.34 – 2.46	~207	0104.D-0605

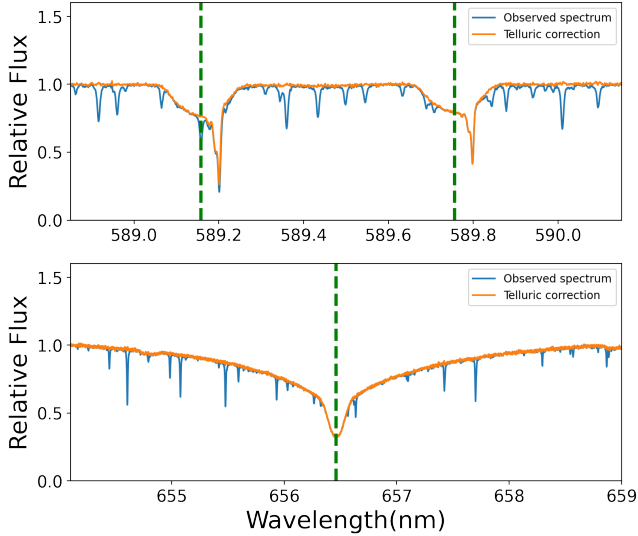


Figure 1. An example of telluric correction using *Molecfit* in the observed spectrum of MASCARA-4b taken in T1 for Na I D1 & D2 (Top) and H α (Bottom). The observed spectra are shown in blue, while the spectra after telluric correction are shown in orange. The dashed green vertical lines represent the static positions of the atomic lines in vacuum.

Na I D1&D2 doublet region (Top panel) and H α spectral line region (Bottom panel), illustrating the goodness of our telluric correction.

3. DATA ANALYSIS

3.1. Transmission spectrum construction

The signal of an exoplanet atmosphere is encoded in transmission spectra of the planet. Following the previous successes in HRS studies, we adopted the similar method outlined in Wyttenbach et al. (2015) and Casasayas-Barris et al. (2019a) to extract transmission spectra for each exposure. After correcting telluric contamination as described in Section 2, all the observed spectra were normalized to their continuum level with the *iSpec* package (Blanco-Cuaresma et al. 2014; Blanco-Cuaresma 2019). We also applied a sigma-clipping rejection algorithm on the normalized spectra and replaced the cosmic ray hits with the mean value of all the other spectra at each wavelength (Allart et al. 2017). Then we shifted the spectra to the stellar rest frame, and constructed a master-out spectrum by cal-

Table 2. Parameters of the MASCARA-4 system.

Description	Symbol	Value
Stellar Parameters		
V magnitude	m_v	8.19 ± 0.01 mag
Effective temp.	T_{eff}	7800 ± 200 K
Surface gravity	$\log g_*$	4.10 ± 0.05 cgs
Metallicity	[Fe/H]	~ 0.00 dex
Stellar mass	M_*	$1.75 \pm 0.05 M_\odot$
Stellar radius	R_*	$1.92 \pm 0.11 R_\odot$
Projected spin	$V \sin i_*$	$45.66^{+1.13}_{-0.9}$ km s $^{-1}$
Planet Parameter		
Planet mass 1	M_p	$1.675 \pm 0.241 M_{\text{Jup}}$
Planet radius 1	R_p	$1.515 \pm 0.044 R_{\text{Jup}}$
Planet density 1	ρ	$0.481^{+0.085}_{-0.079}$ g cm $^{-3}$
Equilibrium temp 1	T_{eq}	2250 ± 62 K
Radius ratio 1	R_p/R_*	$0.08^{+0.004}_{-0.002}$
Orbit Parameters		
Epoch-BJD	T_c	2458505.817 ± 0.003
Period	P	2.82406 ± 0.00003 d
Transit duration	T_{14}	0.165 ± 0.006 d
Semi-major axis	a	0.047 ± 0.004 AU
Inclination	i	88.5 ± 0.01 deg
Semi-amplitude velocity 1	K_p	182 ± 5 km s $^{-1}$

Notes:(1) Zhang et al. (2022). All other parameters refer to Dorval et al. (2020).

culating the average of the aligned out-of-transit spectra with their mean SNR as weights. The master-out spectrum is should be purely stellar origin, and is thus used to divide each individual spectrum in order to remove stellar light contribution so that the absorption signal from the planetary atmosphere may stand out (Stangret et al. 2021). The resulted “divide-out” residual spectra constitute the 2D transmission spectrum map.

3.2. Survey of atoms and molecules using the cross-correlation technique

3.2.1. Template spectra

Zhang et al. (2022) reported excess absorption by H α , H β , Na I D1&D2, Ca II H&K, and strong lines of Mg, Fe and Fe+, and detected the species Mg, Ca, Cr, Fe

and Fe+ using the cross-correlation technique. Given its high equilibrium temperature, we suspected that this planet might also bear heavier species, as found in the atmospheres KELT-9 b, WASP-121 b and WASP-76 b (Hoeijmakers et al. 2019; Ehrenreich et al. 2020; Azevedo Silva et al. 2022). Therefore, we performed a thorough survey of the atoms/ions from Li to U in the atmosphere of MASCARA-4 b in the obtained high-R transmission spectra using the cross-correlation function (CCF) technique. That is to calculate the CCFs of the obtained transmission spectra and the template spectra, following the pioneer works (Snellen et al. 2010; Hoeijmakers et al. 2019). This technique can fully utilize all the spectral signals from multiple lines of a certain species to enhance the detection capability.

The template spectra for a given species or a combination of multiple species in planet atmosphere can be computed by the python package `petitRADTRANS` (Mollière et al. 2019, pRT in short). This package is built for the spectral characterization of exoplanet atmosphere and has been used successfully in many atmospheric studies (e.g. Mollière et al. 2020; Landman et al. 2021; Casasayas-Barris et al. 2022), which requires inputs of parameters of the planet system, a pressure-temperature (TP), and opacities for each species of interests. The planetary and stellar parameters that are required are all included in Table 2. An isothermal pressure-temperature (TP) profile with a temperature of 2500 K is adopted and a solar abundance is assumed for the determination of the volume mixing ratio (VMR) of various species. However, for some species it is not that straightforward to generate their model spectra, because of the lack of corresponding opacities in the pRT database. This prevent a free exploration of any species in the planet atmospheres. Fortunately, the DACE database provides pre-calculated opacities for many neutral and ionized atoms from the element Li to element U. There opacities are generated using the method presented in Grimm & Heng (2015), at a wide temperature range of 2000 K to 6000 K but at a constant pressure of 10^{-8} bar. Kesseli et al. (2022) carried out a comparison study between the pRT pre-computed opacities with those from the DACE opacities, and they concluded that no significant difference in signals should be expected. For comparisons, we perform additional CCF analysis using the DACE opacities for the species with pRT pre-computed opacities available, i.e., Mg, Ca, Cr and Fe. We confirm the conclusion drawn by Kesseli et al. (2022) that both templates yield consistent results, particularly the detection S/Ns and signal’s velocity, as shown in Table 3

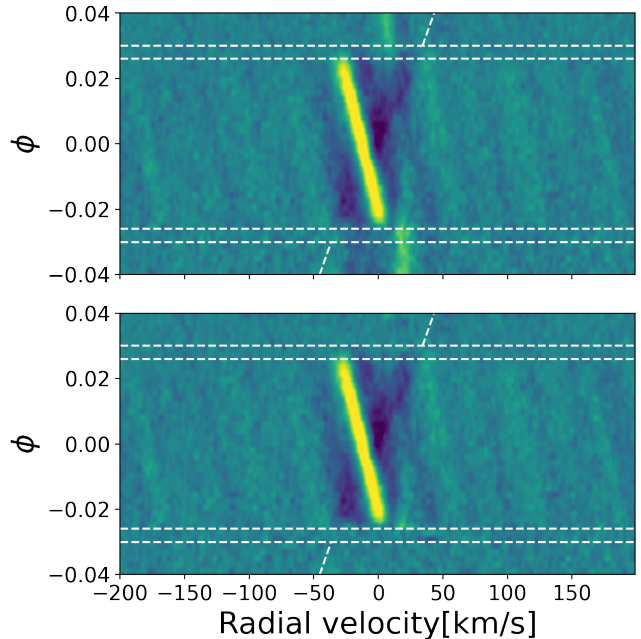


Figure 2. The combined CCF Map at different orbital phase before (*top panel*) and after (*bottom panel*) the correction of stellar pulsation, respectively. The Map is combined with a step size of 0.002 in orbital phase. In each panel, the white dotted lines mark the four contacts during the transit, the inclined white lines indicate the expected trace of signal from the planet, and the bright yellow stripe shows the RM +CLV signal. The out-of-transit steaks in the top panel arise from stellar pulsation.

3.2.2. Cross-correlation analysis

The generated template spectra are then convolved with a Gaussian function to match the resolution of spectra obtained with ESPRESSO. Then, the CCF coefficients between the template spectra and the stellar rest frame residual spectra are calculated using the following formula:

$$c(v, t) = \frac{\sum_i^N x_i(t) T_i(v)}{\sum_i^N T_i(v)}, \quad (1)$$

where $T_i(v)$ is the template shifted to a RV of v , $x_i(t)$ is the transmission spectrum at time t , $c(v, t)$ is a 2-dimensional matrix dependent on t and v . The CCFs are calculated for each residual transmission spectrum and template spectrum, with the latter moving in the RV range of $[-100, 100]$ km s^{-1} with step of 1 km s^{-1} , resulting a 2D residual CCF map as shown in Fig. 2. If the targeted species exists, the signal shall appear as a dark trace along the expected moving direction of the planet in the CCF map, and show at the position of the estimated orbital velocity K_p and system velocity V_{sys} in the $K_p - \Delta V_{\text{sys}}$ map (Hoeijmakers et al. 2019).

To achieve higher signal-to-noise ratios (SNRs) for the purpose of gaining higher detection significance, the CCF maps obtained for T1 & T2 were combined into one CCF map. The CCF spectra in one night are firstly interpolated at a uniform phase grid with a constant step of 0.002, such that the two nights CCF maps are aligned in phase space. Then for each phase, the two interpolated CCF spectra from T1 & T2 are averaged to be the new combined CCF spectrum. Repeating this procedure for each phase, one can obtain the combined CCF map. An example is shown in Figure 2 for the atom Fe. The dark shadow in between the inclined dashed lines represents the absorption of the planet’s atmospheric signal, while the bright stripe is resulted from the center-to-limb (CLV) variation (Yan et al. 2017) and the Rossiter-McLaughlin (RM) effect (Rossiter 1924 and McLaughlin 1924), due to the non-uniform of the brightness in the stellar discs and the differences in the projected RVs at the different distance to the stellar centers.

3.2.3. Stellar pulsations

As shown in the top panel of Figure 2, two bright streaks are visible in the out-of-transit region, which should be caused by the stellar pulsations. Such patterns are also noted in the residual CCF Map of Zhang et al. (2022) and need to be carefully removed. We follow the method presented in Wytttenbach et al. (2020) and Zhang et al. (2022) to empirically mitigated the ripples, assuming that the stellar pulsation feature in each row of the CCF map can be approximately represented by a 1D Gaussian function with constant radial velocity and can be reasonably modelled. The out-of-transit residual CCFs before ingress and after egress are co-added respectively, with the strongest peak fitted by a Gaussian profile. All the individual out-of-transit CCFs are subtracted with the best-fit Gaussian component. We iterate this fitting process seven times until the two streaks are barely visible in the CCF map. As shown in the bottom panel of Figure 2, the out-of-transit pulsation signal is well mitigated, although there still some weak structure remaining in the in-transit region.

3.2.4. Removal of the RM and CLV Effect

The deformation of the stellar line profile caused by CLV and RM effects produce strong signals in the CCF maps (the yellowish bright strip), which mixes with the planet signal and prevents a reliable study on the latter signal. To disentangle the stellar signal from the planetary signal, we follow the method used in Yan & Henning (2018), Chen et al. (2020) and Casasayas-Barris et al. (2019b) to model the stellar spectra at different transit positions. We use the `Spectroscopy`

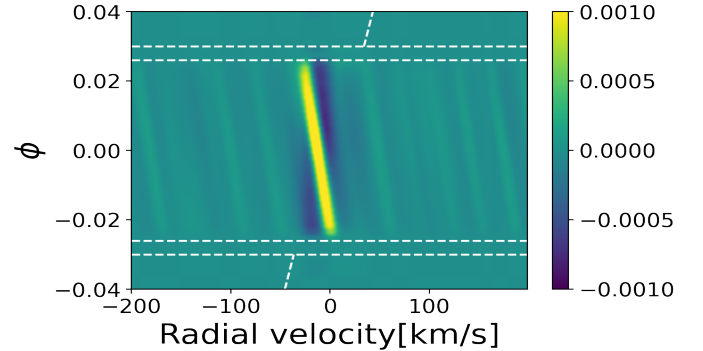


Figure 3. The RM+CLV model for Fe generated by cross-correlation between residual spectra created by synthetic spectrum using SME and the template spectra calculated by DACE, which is used to eliminate the influence of the variation of stellar line profile during transit.

`Made Easy` tool (SME, Valenti & Piskunov 1996) to compute the theoretical stellar spectra at 21 different limb-darkening angles (μ) using the MARCS and VALD3 line lists (Ryabchikova et al. 2015) and employ solar abundance and local thermodynamical equilibrium (LTE) for the calculation of stellar spectra. The stellar disk is divided into small elements with size of $0.01 R_{\star} \times 0.01 R_{\star}$, and each of them owns specific parameters including $v \sin i_{\star}$, μ , and θ (the angle between the normal to each element and the line of sight). The relative position of the planet to the stellar disk is calculated assuming a uniform velocity during the transit. Then, the synthetic spectrum during transit is calculated by summing up the spectra of all the surface elements excluding those obscured by the planet.

The next step is to simulate the RM+CLV effects and correct them. We construct the master out-of-transit spectrum of the synthetic spectrum and divided each synthetic spectrum by it and then cross-correlated with the generated template spectra for each species. The obtained RM+CLV 2D CCF map is to be used as a proxy as shown in the Figure 3, which will be re-scaled to match the observation and subtracted. After the correction, the influence of RM+CLV effect are largely reduced.

4. RESULTS AND DISCUSSION

The obtained transmission spectra are checked visually around the strong individual absorption lines. We confirm that $H\alpha$, $H\beta$, NaI doublet, Ca II doublet, Mg I, Fe I and Fe II do show additional absorption, as claimed by Zhang et al. (2022). The cross-correlation analysis are performed respectively for all the species with available opacities from Li to U generated by DACE, and those covered by pRT using its own database. In Table 3,

Table 3. Summary of the detection derived by DACE and pRT. In the last column, “Confirmative detection” means the species were detected by previous work, and is confirmed in this work; “First detection” means this species is detected for the first time in exoplanets; “New discovery” means this species have been detected in other exoplanets but new in MASCARA-4b, and this work present the first detection of this species in MASCARA-4b.

Species	Template Type	Peak S/N	Amplitude ppm	K_p km s ⁻¹	V_{shifted} km s ⁻¹	FWHM km s ⁻¹	Remarks
Mg	pRT	6.1	1387.82 ± 108.0	147.59 ± 28.06	-0.8 ± 1.91	11.63 ± 0.34	Confirmative detection
	DACE	7.3	2632.80 ± 176.0	163.59 ± 24.94	0.6 ± 1.88	13.68 ± 0.33	
Ca	pRT	5.2	162.86 ± 18.4	198.59 ± 22.20	-11.8 ± 2.88	14.96 ± 0.47	Confirmative detection
	DACE	5.2	376.05 ± 36.7	186.59 ± 27.48	-10.3 ± 3.48	18.17 ± 0.48	
Cr	pRT	7.4	2084.84 ± 183.0	201.59 ± 18.18	-2.2 ± 2.34	17.24 ± 0.52	Confirmative detection
	DACE	6.5	1108.44 ± 80.50	223.59 ± 30.00	-11.6 ± 2.95	19.00 ± 0.46	
Fe	pRT	14.0	6096.99 ± 296.0	181.59 ± 14.02	-1.1 ± 0.92	12.87 ± 0.24	Confirmative detection
	DACE	14.9	5827.07 ± 265.0	195.59 ± 12.72	-2.2 ± 0.92	13.66 ± 0.23	
Rb	DACE	5.9	145.03 ± 12.80	183.59 ± 24.14	-3.8 ± 3.28	19.32 ± 0.62	First detection
Sm	DACE	5.1	170.66 ± 17.2	205.59 ± 23.75	-3.4 ± 3.53	17.84 ± 0.52	First detection
Ti+	DACE	7.9	3059.07 ± 233.0	175.59 ± 17.98	-1.1 ± 1.53	11.67 ± 0.35	New discovery
Ba+	DACE	5.5	61.52 ± 4.64	169.59 ± 55.40	-1.4 ± 7.49	41.35 ± 0.83	New discovery
Sc+	DACE	6.4	622.73 ± 35.9	219.59 ± 32.75	-22.3 ± 3.89	25.01 ± 0.42	Tentative detection

we list all the species with absorption features detected with peak S/Ns > 5. As discussed in Section 3.2.1, the results using different sources of opacities are consistent with each other. We confirm from Fig. 4 and Fig. 6 clear detection of Mg, Ca, Cr and Fe firstly reported by Zhang et al. (2022). The detection significance, i.e., the S/N values, of Mg, Ca and Cr in this work are well consistent with those in Zhang et al. (2022). However our detection S/N of Fe in the CCF map is obviously smaller than that in Zhang et al. (2022), but is consistent with their obtained values using individual strong lines (cf. their Table 3.)

In Figures 4 & 6, each row contains 4 panels figures for one species. The first and second panels show the 2D CCF maps for each species before and after the CLV+RM correction, respectively, where the inclined white dashed lines indicate the expected track of planet signal. Note that the left-inclined bright yellow stripe is the CLV+RM signals; the third panel is the $K_p - \Delta V_{\text{sys}}$ map, created by co-adding CCFs assuming a range of K_p and ΔV_{sys} , where K_p is the Keplerian speed of the planet and is estimated to be ~ 182 km s⁻¹ by Zhang et al. (2022) while ΔV_{sys} is the velocity relative to the planet rest frame. In such maps, signal from the planet should be the strongest around the expected K_p and ΔV_{sys} , i.e., at the intersection of white dashed lines. The red cross marks the position with maximum SNR, which do not always coincide well with the intersection point. Gaussian fits using the python module `lmfit` are applied on the horizontal and vertical slices pass-

ing the red cross to the determine the peak positions in ΔV_{sys} and K_p , respectively, as well as the FWHM of the detected signals. The best-fit parameters are listed in Table 3, together with their uncertainties calculated adopting the method described in Kesseli et al. (2022). The fourth panel shows the SNR profile of the corresponding species against different ΔV_{sys} , either at the expected K_p (the blue line), or at the K_p with maximum SNR (the orange line), respectively.

As expected, we detect several heavier species in the atmosphere of MASCARA-4 b, including Rb, Sm, Ti+ and Ba+ with SNR > 5 and reasonable offsets of K_p and ΔV_{sys} , as shown in Fig. 7 and Table 3. This is the first time that the element Rb (Rubidium) is detected in the atmosphere of exoplanet. Rb is an alkali metal similar to Na and K with atomic number 37, and is the most electropositive just after Caesium (Cs). Ba+ was firstly detected in two UHJs by Azevedo Silva et al. (2022), and this work presents the third detection, giving solid support to the popular presence of Ba+ in UHJs. Ti+ was detected in KELT-9 b (Hoeijmakers et al. 2018) and WASP-189 b (Prinoth et al. 2022), and was tentatively detected in WASP121 b (Azevedo Silva et al. 2022) and WASP-33 b (Cont et al. 2022), and is robustly detected in MASCARA-4 b with high significance and small offsets. We also use the pRT to search for the molecules CaH, FeH, VO and TiO as shown in the Figure 5. They all strongly absorb ultra-violet and visible light and would heat the upper atmosphere, leading to a rise in temperature with altitude, called as the thermal in-

version (Knutson et al. 2008; Merritt et al. 2020). No signals from them are detected in this planet.

In addition, we report tentative detection of Sc+, with a peak SNR value about 6.4 but deviating far from the estimated position, with a relatively large K_p and ΔV_{sys} , as shown in Fig. 7 and Table 3. The species Sc+ was detected previously in several UHJs, e.g., KELT-9 b (Hoeijmakers et al. 2018). The common presence of those heavy ions (Ti+, Ba+, Sc+) at high altitudes in UHJ's implies that such kind of planets may experience atmospheric dynamics that we currently do not expect. From Fig. 4, 6, 7 and Table 3, all the detected species excepting for Sc+ are blue-shifted by about 0 to 10 km s^{-1} as observed in the same target by Zhang et al. (2022) and in WASP76 b and WASP121 b by Azevedo Silva et al. (2022). Such phenomena is widely recognized as the result of the eastern wind across the terminator region of a tidally-locked planet.

Finally, it is quite interesting to note the new detection of Sm (samarium), a lanthanide series element with atom number of 62. Sm is detected with peak SNR about 5.1 with velocity close to the planet V_{sys} , and is likely to a real detection. If confirmed, this will be the first lanthanide series element that has been detected in exoplanets, and is the heaviest element found so far. To summarize, all the Period 4 elements until Ni, plus several Period 5 and 6 metals have been detected in the atmospheres of UHJs. It is the right time to call for

detailed atmospheric modeling to understand how these atoms and ions are populated at high altitudes. On the other hand, higher precision HRS studies should be further conducted on UHJs to reveal the presence of additional species and even some relatively abundant minor isotopes. Perhaps more importantly, retrieval analysis should be performed on the high-resolution transmission spectra to determine the abundance ratio of different elements, which when compared with those of their host stars, should shed light in the understanding of the formation and evolution of planets and their atmospheres.

5. ACKNOWLEDGMENTS

We thank the anonymous reviewer for their constructive comments. This research is supported by the National Natural Science Foundation of China grants No. 11988101, 42075123, 42005098, 62127901, 12273055, 11973048, 11927804, the National Key R&D Program of China No. 2019YFA0405102, the Strategic Priority Research Program of Chinese Academy of Sciences, Grant No. XDA15072113, the China Manned Space Project with NO. CMS-CSST-2021-B12. MZ, YQS are supported by the Chinese Academy of Sciences (CAS), through a grant to the CAS South America Center for Astronomy (CASSACA) in Santiago, Chile.

REFERENCES

- Allart, R., Lovis, C., Pino, L., et al. 2017, *A&A*, 606, A144, doi: [10.1051/0004-6361/201730814](https://doi.org/10.1051/0004-6361/201730814)
- Azevedo Silva, T., Demangeon, O. D. S., Santos, N. C., et al. 2022, *A&A*, 666, L10, doi: [10.1051/0004-6361/202244489](https://doi.org/10.1051/0004-6361/202244489)
- Blanco-Cuaresma, S. 2019, *MNRAS*, 486, 2075, doi: [10.1093/mnras/stz549](https://doi.org/10.1093/mnras/stz549)
- Blanco-Cuaresma, S., Soubiran, C., Heiter, U., & Jofré, P. 2014, *A&A*, 569, A111, doi: [10.1051/0004-6361/201423945](https://doi.org/10.1051/0004-6361/201423945)
- Broggi, M., & Line, M. R. 2019, *AJ*, 157, 114, doi: [10.3847/1538-3881/aaffd3](https://doi.org/10.3847/1538-3881/aaffd3)
- Casasayas-Barris, N., Pallé, E., Yan, F., et al. 2019a, *A&A*, 628, A9, doi: [10.1051/0004-6361/201935623](https://doi.org/10.1051/0004-6361/201935623)
- . 2019b, *A&A*, 628, A9, doi: [10.1051/0004-6361/201935623](https://doi.org/10.1051/0004-6361/201935623)
- Casasayas-Barris, N., Borsa, F., Palle, E., et al. 2022, *A&A*, 664, A121, doi: [10.1051/0004-6361/202143016](https://doi.org/10.1051/0004-6361/202143016)
- Chen, G., Casasayas-Barris, N., Pallé, E., et al. 2020, *A&A*, 635, A171, doi: [10.1051/0004-6361/201936986](https://doi.org/10.1051/0004-6361/201936986)
- Cont, D., Yan, F., Reiners, A., et al. 2022, *A&A*, 668, A53, doi: [10.1051/0004-6361/202244277](https://doi.org/10.1051/0004-6361/202244277)
- Dorval, P., Talens, G. J. J., Otten, G. P. P. L., et al. 2020, *A&A*, 635, A60, doi: [10.1051/0004-6361/201935611](https://doi.org/10.1051/0004-6361/201935611)
- Ehrenreich, D., Lovis, C., Allart, R., et al. 2020, *Nature*, 580, 597, doi: [10.1038/s41586-020-2107-1](https://doi.org/10.1038/s41586-020-2107-1)
- Grimm, S. L., & Heng, K. 2015, *ApJ*, 808, 182, doi: [10.1088/0004-637X/808/2/182](https://doi.org/10.1088/0004-637X/808/2/182)
- Hoeijmakers, H. J., Ehrenreich, D., Heng, K., et al. 2018, *Nature*, 560, 453, doi: [10.1038/s41586-018-0401-y](https://doi.org/10.1038/s41586-018-0401-y)
- Hoeijmakers, H. J., Ehrenreich, D., Kitzmann, D., et al. 2019, *A&A*, 627, A165, doi: [10.1051/0004-6361/201935089](https://doi.org/10.1051/0004-6361/201935089)
- Kausch, W., Noll, S., Smette, A., et al. 2015, *A&A*, 576, A78, doi: [10.1051/0004-6361/201423909](https://doi.org/10.1051/0004-6361/201423909)
- Kempton, E. M. R., Bean, J. L., Louie, D. R., et al. 2018, *PASP*, 130, 114401, doi: [10.1088/1538-3873/aadf6f](https://doi.org/10.1088/1538-3873/aadf6f)
- Kesseli, A. Y., Snellen, I. A. G., Casasayas-Barris, N., Mollière, P., & Sánchez-López, A. 2022, *AJ*, 163, 107, doi: [10.3847/1538-3881/ac4336](https://doi.org/10.3847/1538-3881/ac4336)

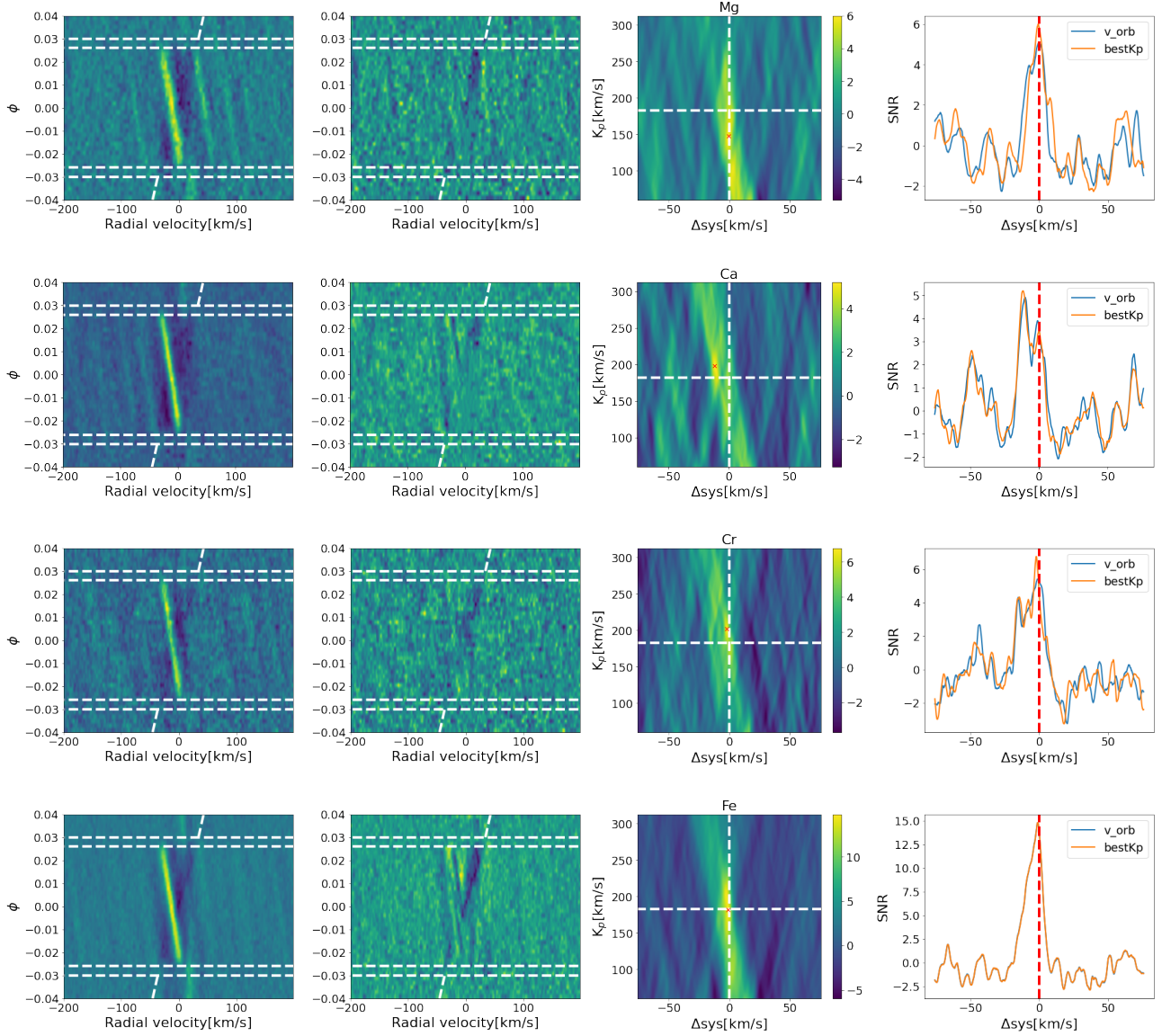


Figure 4. *First panels:* The 2D CCF maps of Mg, Ca, Cr and Fe with CLV+RM effects uncorrected using pRT opacity. The white dotted lines mark the beginning and ending positions of the transit and the inclined white lines indicate the expected trace of signal from the planet. *Second panels:* Same as *the first panels* but with CLV+RM effects corrected. *Third panels:* the K_p - ΔV_{sys} maps in the range of $50 \sim 300 \text{ km s}^{-1}$. In each panel, the planet signal is expected to appear around the intersection of the two white dotted lines, while the red crosses marks the position with maximum SNR. *Fourth panels:* the SNR plots at the expected K_p position in blue and at the Max-SNR corresponding K_p .

Kirk, J., Alam, M. K., López-Morales, M., & Zeng, L. 2020, *AJ*, 159, 115, doi: [10.3847/1538-3881/ab6e66](https://doi.org/10.3847/1538-3881/ab6e66)

Knutson, H. A., Charbonneau, D., Allen, L. E., Burrows, A., & Megeath, S. T. 2008, *ApJ*, 673, 526, doi: [10.1086/523894](https://doi.org/10.1086/523894)

Landman, R., Sánchez-López, A., Mollière, P., et al. 2021, *A&A*, 656, A119, doi: [10.1051/0004-6361/202141696](https://doi.org/10.1051/0004-6361/202141696)

McLaughlin, D. B. 1924, *ApJ*, 60, 22, doi: [10.1086/142826](https://doi.org/10.1086/142826)

Merritt, S. R., Gibson, N. P., Nugroho, S. K., et al. 2020, *A&A*, 636, A117, doi: [10.1051/0004-6361/201937409](https://doi.org/10.1051/0004-6361/201937409)

Mollière, P., Wardenier, J. P., van Boekel, R., et al. 2019, *A&A*, 627, A67, doi: [10.1051/0004-6361/201935470](https://doi.org/10.1051/0004-6361/201935470)

Mollière, P., Stolker, T., Lacour, S., et al. 2020, *A&A*, 640, A131, doi: [10.1051/0004-6361/202038325](https://doi.org/10.1051/0004-6361/202038325)

Pepe, F., Cristiani, S., Rebolo, R., et al. 2021, *A&A*, 645, A96, doi: [10.1051/0004-6361/202038306](https://doi.org/10.1051/0004-6361/202038306)

Prinoth, B., Hoeijmakers, H. J., Kitzmann, D., et al. 2022, *Nature Astronomy*, 6, 449, doi: [10.1038/s41550-021-01581-z](https://doi.org/10.1038/s41550-021-01581-z)

Rossiter, R. A. 1924, *ApJ*, 60, 15, doi: [10.1086/142825](https://doi.org/10.1086/142825)

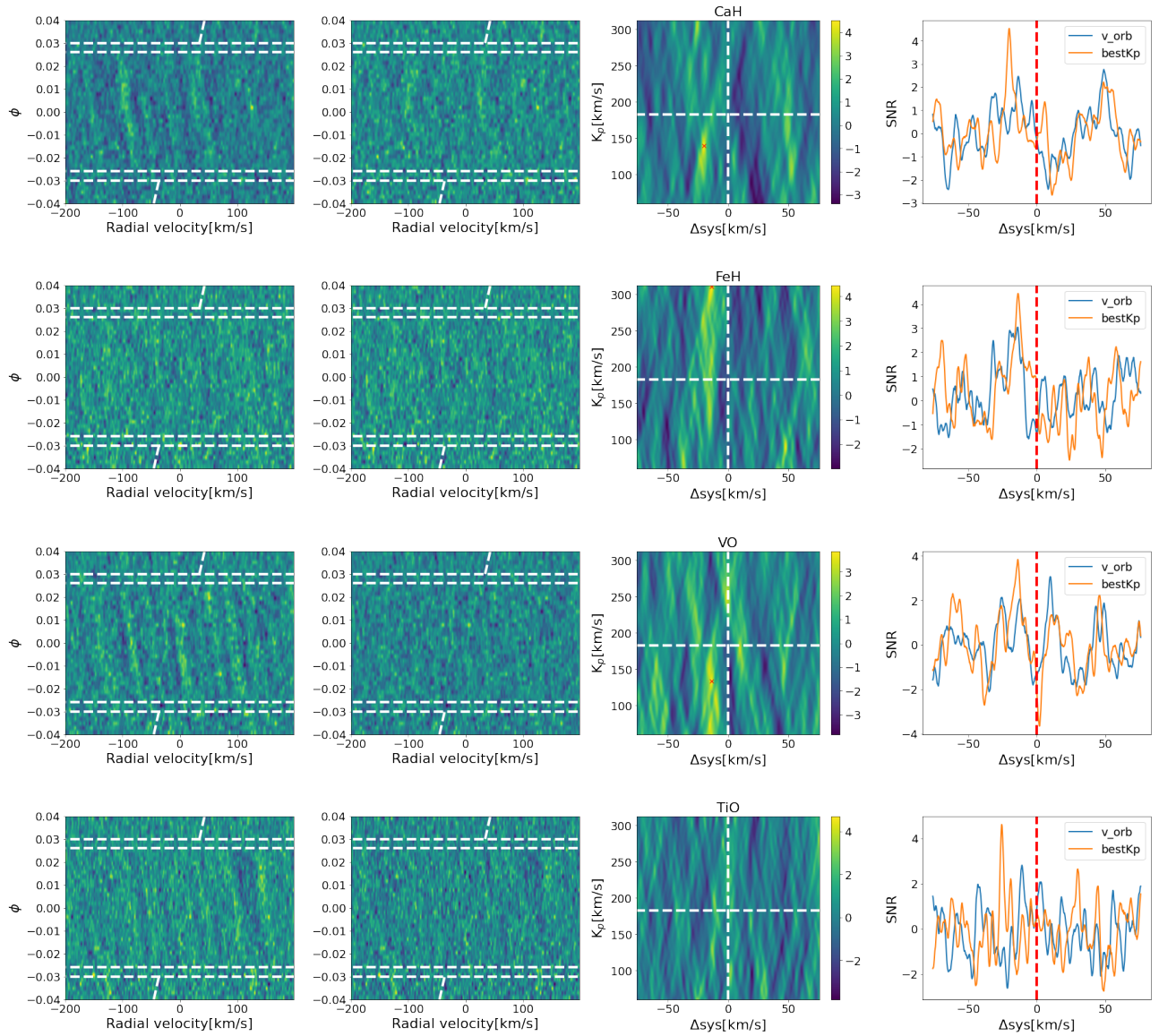


Figure 5. Same as Fig 4: but for CaH, FeH, VO and TiO.

Ryabchikova, T., Piskunov, N., Kurucz, R. L., et al. 2015, *PhyS*, 90, 054005, doi: [10.1088/0031-8949/90/5/054005](https://doi.org/10.1088/0031-8949/90/5/054005)

Seidel, J. V., Ehrenreich, D., Bourrier, V., et al. 2020, *A&A*, 641, L7, doi: [10.1051/0004-6361/202038497](https://doi.org/10.1051/0004-6361/202038497)

Smette, A., Sana, H., Noll, S., et al. 2015, *A&A*, 576, A77, doi: [10.1051/0004-6361/201423932](https://doi.org/10.1051/0004-6361/201423932)

Snellen, I. A. G., de Kok, R. J., de Mooij, E. J. W., & Albrecht, S. 2010, *Nature*, 465, 1049, doi: [10.1038/nature09111](https://doi.org/10.1038/nature09111)

Stangret, M., Pallé, E., Casasayas-Barris, N., et al. 2021, *A&A*, 654, A73, doi: [10.1051/0004-6361/202040100](https://doi.org/10.1051/0004-6361/202040100)

Talens, G. J. J., Albrecht, S., Spronck, J. F. P., et al. 2017, *A&A*, 606, A73, doi: [10.1051/0004-6361/201731282](https://doi.org/10.1051/0004-6361/201731282)

Valenti, J. A., & Piskunov, N. 1996, *A&AS*, 118, 595

Wytenbach, A., Ehrenreich, D., Lovis, C., Udry, S., & Pepe, F. 2015, *A&A*, 577, A62, doi: [10.1051/0004-6361/201525729](https://doi.org/10.1051/0004-6361/201525729)

Wytenbach, A., Mollière, P., Ehrenreich, D., et al. 2020, *A&A*, 638, A87, doi: [10.1051/0004-6361/201937316](https://doi.org/10.1051/0004-6361/201937316)

Yan, F., & Henning, T. 2018, *Nature Astronomy*, 2, 714, doi: [10.1038/s41550-018-0503-3](https://doi.org/10.1038/s41550-018-0503-3)

Yan, F., Pallé, E., Fosbury, R. A. E., Petr-Gotzens, M. G., & Henning, T. 2017, *A&A*, 603, A73, doi: [10.1051/0004-6361/201630144](https://doi.org/10.1051/0004-6361/201630144)

Zhang, Y., Snellen, I. A. G., Wytenbach, A., et al. 2022, *A&A*, 666, A47, doi: [10.1051/0004-6361/202244203](https://doi.org/10.1051/0004-6361/202244203)

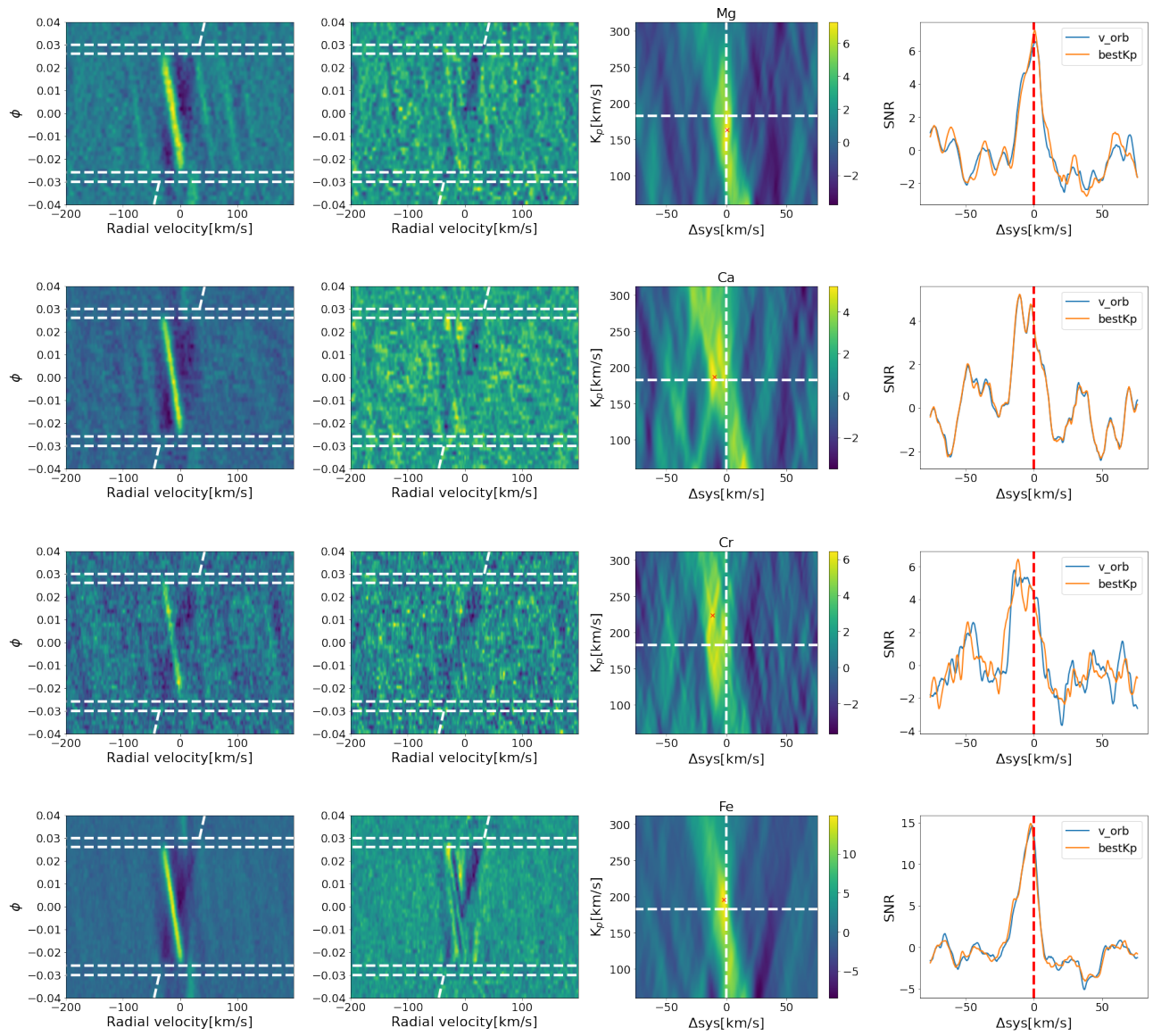


Figure 6. Same as Fig 4: but using DACE opacity to obtain CCFs map for Mg, Ca, Cr and Fe.

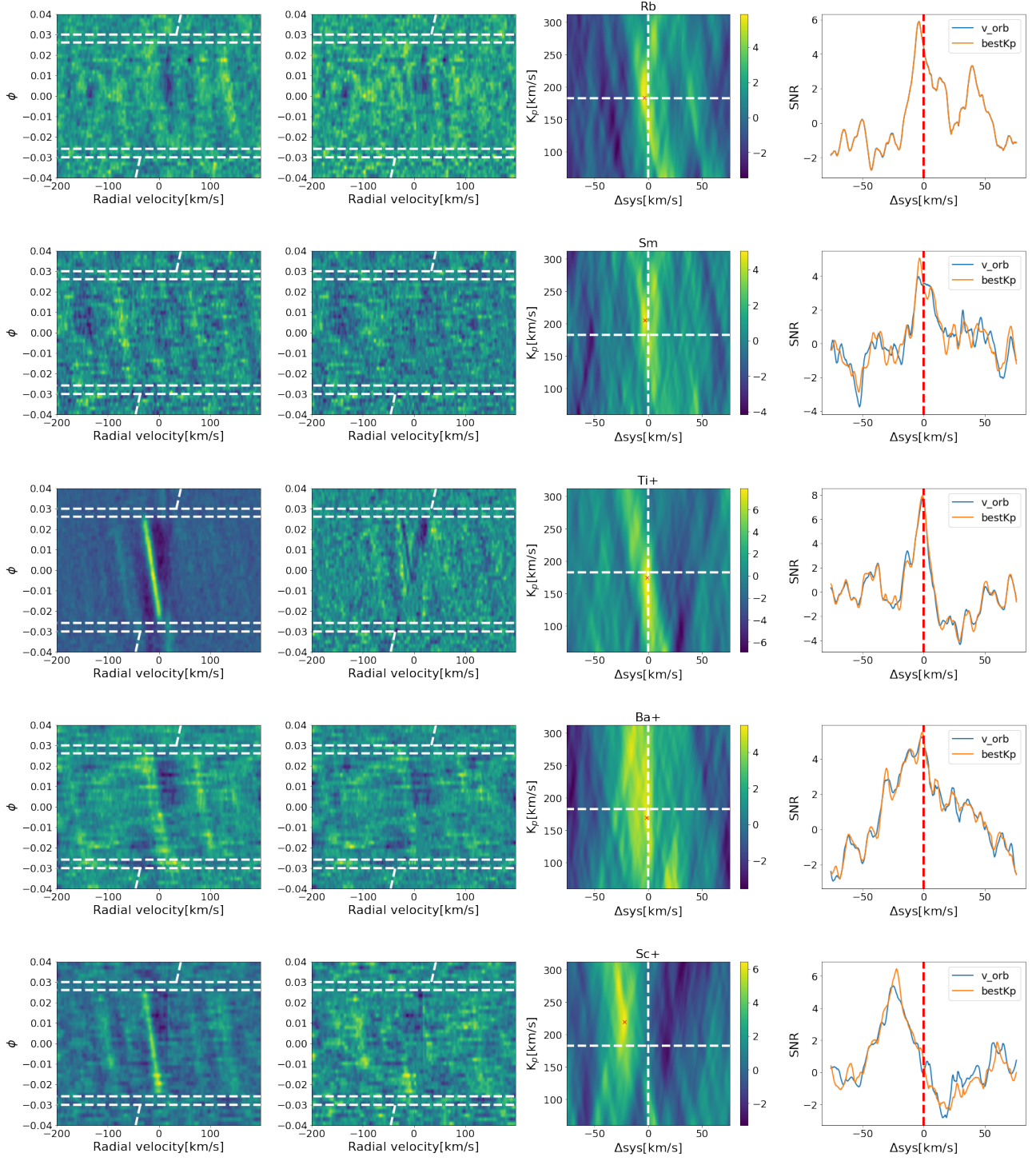


Figure 7. Same as Fig 6: but for Rb, Sm, Ti+, Ba+ and Sc+.